

Hard x-ray photoelectron spectroscopy of tunable oxide interfaces ^F


Cite as: J. Vac. Sci. Technol. A **40**, 013215 (2022); <https://doi.org/10.1116/6.0001491>

Submitted: 26 September 2021 • Accepted: 23 November 2021 • Published Online: 27 December 2021

 Martina Müller,  Patrick Lömker,  Paul Rosenberger, et al.

COLLECTIONS

Paper published as part of the special topic on [Commemorating the Career of Charles S. Fadley](#)

 This paper was selected as Featured



View Online



Export Citation



CrossMark

ARTICLES YOU MAY BE INTERESTED IN

[Prospects for the expansion of standing wave ambient pressure photoemission spectroscopy to reactions at elevated temperatures](#)

Journal of Vacuum Science & Technology A **40**, 013207 (2022); <https://doi.org/10.1116/6.0001353>


[In situ x-ray photoelectron spectroscopy analysis of electrochemical interfaces in battery: Recent advances and remaining challenges](#)

Journal of Vacuum Science & Technology A **40**, 010808 (2022); <https://doi.org/10.1116/6.0001460>


[Practical guides for x-ray photoelectron spectroscopy: Quantitative XPS](#)

Journal of Vacuum Science & Technology A **38**, 041201 (2020); <https://doi.org/10.1116/1.5141395>





HIDEN
ANALYTICAL



40 YEARS
1982 - 2022


Instruments for Advanced Science

- Knowledge,
- Experience,
- Expertise

Click to view our product catalogue


Contact Hiden Analytical for further details:
www.HidenAnalytical.com
info@hideninc.com

Gas Analysis




- ▶ dynamic measurement of reaction gas streams
- ▶ catalysis and thermal analysis
- ▶ molecular beam studies
- ▶ dissolved species probes
- ▶ fermentation, environmental and ecological studies

Surface Science




- ▶ UHVTPD
- ▶ SIMS
- ▶ end point detection in ion beam etch
- ▶ elemental imaging - surface mapping

Plasma Diagnostics



- ▶ plasma source characterization
- ▶ etch and deposition process reaction kinetic studies
- ▶ analysis of neutral and radical species

Vacuum Analysis



- ▶ partial pressure measurement and control of process gases
- ▶ reactive sputter process control
- ▶ vacuum diagnostics
- ▶ vacuum coating process monitoring







Hard x-ray photoelectron spectroscopy of tunable oxide interfaces

Cite as: J. Vac. Sci. Technol. A 40, 013215 (2022); doi: 10.1116/6.0001491

Submitted: 26 September 2021 · Accepted: 23 November 2021 ·

Published Online: 27 December 2021



Martina Müller,^{1,a)}  Patrick Lömker,^{2,3}  Paul Rosenberger,^{1,4,5}  Mai Hussein Hamed,^{6,7}  David N. Mueller,⁵ 
Ronja A. Heinen,⁵ Thomas Szyjka,^{1,5}  and Lutz Baumgarten⁵ 

AFFILIATIONS

¹Fachbereich Physik, Universität Konstanz, 78457 Konstanz, Germany

²Deutsches Elektronen-Synchrotron, Notkestraße 85, 22607 Hamburg, Germany

³Department of Physics, Stockholm University, 10691 Stockholm, Sweden

⁴Fakultät Physik, Technische Universität Dortmund, 44221 Dortmund, Germany

⁵Forschungszentrum Jülich GmbH, Peter Grünberg Institut (PGI-6), 52425 Jülich, Germany

⁶Jülich Centre for Neutron Science (JCNS-2) and Peter Grünberg Institut (PGI-4), JARA-FIT, Forschungszentrum Jülich GmbH, 52425 Jülich, Germany

⁷Faculty of Science, Helwan University, Cairo 11795, Egypt

Note: This paper is a part of the Special Collection Commemorating the Career of Charles S. Fadley.

Electronic mail: martina.mueller@uni.kn

ABSTRACT

The tunability of the oxygen content in complex oxides and heterostructures has emerged as a key to designing their physical functionalities. Controlling the interface reactivity by redox reactions provides a powerful means to deliberately set distinct oxide phases and emerging properties. We present routes on how to control oxygen-driven redox mechanisms in ultrathin ferro(i)magnetic and ferroelectric oxide films and across oxide interfaces. We address the growth and control of metastable EuO oxide phases, the control of phase transitions of binary Fe oxides by oxygen migration, the *in operando* determination of NiFe₂O₄/SrTiO₃ interface band alignments, as well as the role of interfacial oxide exchange in ferroelectric HfO₂-based capacitors—uncovered by the unique capabilities of photoelectron spectroscopy and, in particular, using hard x-rays.

© 2021 Author(s). All article content, except where otherwise noted, is licensed under a Creative Commons Attribution (CC BY) license (<http://creativecommons.org/licenses/by/4.0/>). <https://doi.org/10.1116/6.0001491>

I. INTRODUCTION

The last decade has witnessed that physical functionalities of ultrathin solid films are not only controlled by their bulk electronic structure but, to a significant extent, by their interfaces.^{1,2} In metal oxides, the tunability of the oxygen content represents the crucial degree of freedom, which enables us to design material functionalities beyond, e.g., the property portfolio of semiconductors.³ Whether oxygen ions are present or absent in the lattice can either be a mandatory prerequisite or detrimental for the emergence of oxide properties, and may actually induce new ones.⁴ If metal oxide thin films are joined in a heterostructure, thermodynamic and electrochemical nonequilibrium conditions may drive atom and charge exchange across their contacting interfaces. Interface chemical

reactions will occur in the case of oxygen transport; charge transfer is promoted by compensating different contact potentials.

In particular, with regard to reduction-oxidation reactions, the importance of the choice of oxide substrate materials has typically been downplayed. Only lately, the huge potential of this determining factor was received for the design of oxide functionalities via interfacial oxide exchange, such as magnetic or ferroelectric oxides.^{5,6} The impact of the presence or absence of oxygen is, however, antagonistic: While oxygen ions are an inevitable part of the complex exchange mechanisms in magnetic oxides⁷ and their absence leads to a degrading of properties, oxygen vacancies have been identified to induce ferroelectricity in dielectric oxides.⁸ Here, a well-balanced presence of vacancies can stabilize a robust

ferroelectric state over thousands of electric field switching cycles.⁶ Exploiting the tunability of the oxygen content in the materials themselves and understanding interface formation are versatile strategies in designing new functional properties through controlled interfacial oxygen exchange.

X-ray photoelectron spectroscopy (XPS) has been developed as one of the most powerful tools to explore the chemical composition and electronic structure of solids.^{9,10} While the probing depth of XPS using laboratory x-ray sources is well suited for studying the subsurface region of an ultrathin film (about 3–5 nm), the photoelectron information depth is significantly enhanced to about 20–30 nm by performing spectroscopy in the hard x-ray regime (HAXPES).¹¹ The strongly reduced photoelectron cross sections at high photon energies are compensated by high brilliance beamlines optimized for HAXPES. Hence, the combination of soft- and hard x-ray photoelectron spectroscopy provides the opportunity to element-selectively monitor the redox-driven chemical states, electronic and electrostatic properties of oxide thin films, heterostructures, and buried interfaces.

Moreover, HAXPES allows for a nondestructive depth profiling by varying either the photon excitation energy or photoelectron emission angle.⁹ A quantification of stoichiometry via chemical binding energy shifts is possible down to a few percent, which permits uncovering redox processes by valence changes of oxide phases.¹² The spectroscopic signatures of oxygen vacancies are of indirect nature though and only become apparent by rigid binding energy shifts of core levels, which are caused by changes of the Fermi level position in an altered local electric potential. This approach is also used in the so-called Kraut method, which is successfully applied to derive the band alignment at metal oxide/semiconductor interfaces, provided that there are no chemical reactions.¹³ For such samples, the variant of *in operando* HAXPES becomes applicable, which serves as a powerful tool to determine the band alignment and the chemical state of (oxide) interfaces under operation conditions of an electric device in a single measurement.

This article highlights research examples for which laboratory- and synchrotron-based photoelectron spectroscopy emerged as the key experimental probe to uncover complex oxygen exchange mechanisms in oxide ultrathin films and at oxide interfaces, as schematically depicted in Fig. 1. In particular, emerging interface states and their tunability in ferro(i)magnetic and ferroelectric oxide heterostructures—covering both fundamental aspects and exploring application-relevant devices—are discussed.

II. REDOX-ASSISTED GROWTH AT METASTABLE OXIDE INTERFACES

In Sec. II A, we present selected examples of how laboratory- and synchrotron-based XPS enables stabilizing the physically exceptionally versatile though metastable europium monoxide as ultrathin films in all-oxide heterostructures. EuO is a prototype Heisenberg ferromagnet with a spin-only magnetic moment of $S = 7/2$ and semiconducting properties.⁷ This rare combination has led to numerous past and recent works on the fundamental spin-dependent electronic properties.^{14–16} In particular, interfacing EuO to oxides and metals gives rise to emerging quantum states, which origin either from atomic-scale interface growth control or are

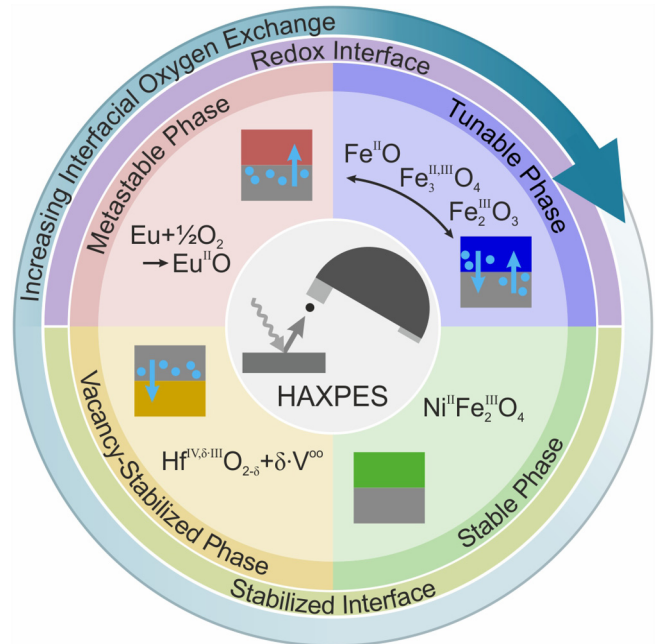


FIG. 1. Tunability of complex oxides heterostructures by interfacial oxygen exchange. Redox-active oxide interfaces allow for a growth-controlled stabilization of metastable phases (EuO) or enable even fully reversible phase transitions (Fe_3O_4). Thermodynamically less active interfaces, in contrary, can promote vacancy-stabilized phases (HfO_2) or interfaces with negligible oxygen exchange (NiFe_2O_4).

induced by proximity effects at well-defined interfaces. Recent examples include the emergence of two-dimensional electron systems,^{17,18} interfacial spin-charge conversion,¹⁹ or induced ferroelectric states.²⁰

Although being particularly prominent as the Heisenberg model system, the growth of EuO single-crystalline and ultrathin films is exceptionally challenging because Eu^{2+}O is the metastable suboxide of europium—in contrast to its stable but paramagnetic counterpart $\text{Eu}_2^{3+}\text{O}_3$. Both a meticulous control over the oxygen backpressure during Eu deposition and the finding that small excesses of Eu metal on hot substrate surfaces are tolerable have enabled the so-called “distillation” growth of stoichiometric EuO on inert substrates.²¹ Not surprisingly, growing EuO on oxide substrates further complicates the synthesis because the interface also needs to be taken into account as a potential oxygen source or sink. Hence, the oxygen-related interface thermodynamics and kinetics strongly determine the EuO film and interface properties as a direct consequence of the growth process.²² To gain a fundamental understanding of the growth-dependent evolution of this metastable oxide interface, the proceeding EuO deposition process and growth-related interface formation are tracked by *in situ* XPS.

A. EuO/YSZ: A quasi-inert “model” interface?

EuO on yttria-stabilized zirconia (YSZ) is typically regarded as a model system because YSZ (001) and EuO (001) are

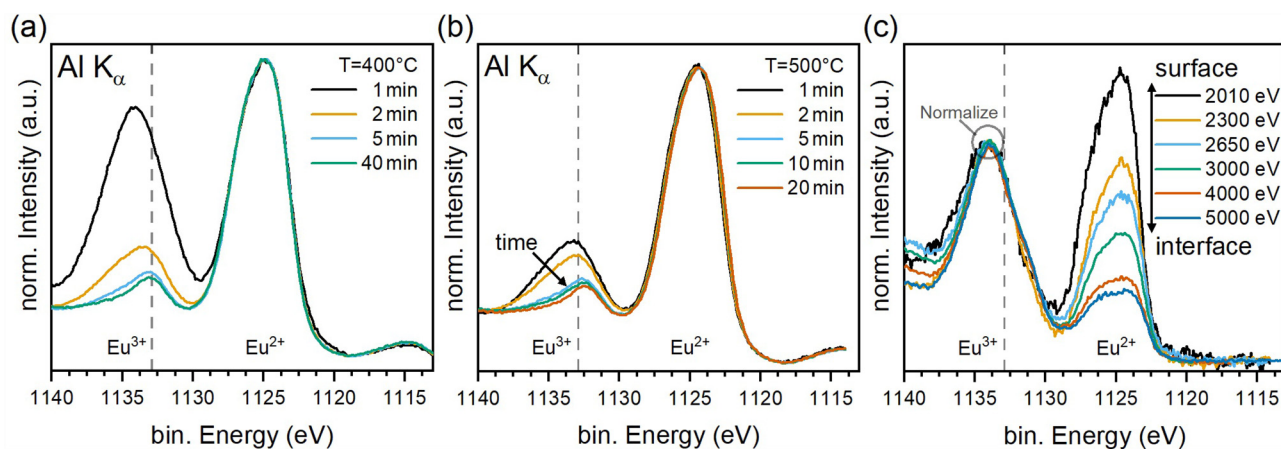


FIG. 2. (a) XPS of the Eu $3d_{5/2}$ core level of EuO/YSZ films synthesized by depositing metal only for several deposition times. (b) Lab depth-resolved XPS of an EuO/SrTiO₃ bilayer. (c) Depth profile of a buffered oxide interface system obtained using HAXPES at KMC-1 (BESSY-II). The content of Eu²⁺ increases toward the surface, this is caused by a combination of oxygen mobility and thermodynamic potential through the complex YSZ/ITO interface.

lattice-matched, and the interface is usually assumed to be quasi-inert, which should result in both structurally and chemically well-defined film/substrate interface.²¹ This assumption is corroborated by a thermodynamic Ellingham analysis, which is, however, strictly valid for bulklike systems only.²³

Here, we focus on the regime of ultrathin EuO films with thicknesses of a few monolayers deposited by molecular beam epitaxy (MBE). By using *in situ* lab-based XPS (Al K_{α}), we probe the stoichiometry of the first monolayers of EuO at the EuO/YSZ interface. Without adding any additional oxygen gas, the Eu metal deposition duration was varied between 1 and 40 min at a substrate temperature $T_s = 400^\circ\text{C}$. We developed a lab-based strategy for nondestructive depth profiling, i.e., monolayer-controlled Eu deposition is performed stepwise and alternated with *in situ* XPS analysis.

The corresponding Eu $3d_{5/2}$ spectra for 1, 2, 5, and 40 min of Eu deposition are shown in Fig. 2(a). For 1 and 2 min, we find a significant ratio of Eu³⁺ contributing to the spectrum. After 5 min, the Eu³⁺ ratio is drastically reduced but still clearly observable, while after 40 min, the spectrum shows a pure Eu²⁺ signal.

Observing Eu³⁺ in the initial phase of the growth process indicates the unexpected formation of Eu₃O₄ or Eu₂O₃ at the EuO/YSZ interface—which is typically glossed over. Obviously, the thermodynamic landscape of the YSZ interface favors the formation of oxygen vacancies, which on the other hand supplies oxygen to the deposited EuO film.²⁴ This finding clearly demonstrates that indeed a limited oxygen supply is provided by the YSZ template, which oxidizes EuO to Eu₃O₄ or Eu₂O₃—thereby bypassing the thermodynamical prediction for chemically stable bulk EuO/YSZ.²³ Overcoming this phenomenon by, e.g., adopted growth parameters, allows for synthesizing ultrathin EuO films by depositing Eu metal *even without* externally supplied oxygen on YSZ. Such “redox-assisted” growth may enable us to stabilize otherwise metastable oxide interfaces in a straightforward and well-controllable manner. Depending on the specific oxygen ion conductivity of the oxide

substrate, the film thickness also becomes well-adjustable by this redox-assisted growth process, as will be discussed in the following.

B. EuO/SrTiO₃ : The well-controllable redox interface

Using the previously acquired knowledge on the EuO/YSZ interface, we extend our study to the well-known “work-horse” of oxide electronics, SrTiO₃ (STO). Applying the thermodynamical Ellingham analysis, we learn that SrTiO₃ and EuO shall *not* coexist and that we ought to expect Eu₂O₃ formation. In order to track the oxygen supply at the EuO/SrTiO₃ interface, we deposited the Eu metal at $T = 500^\circ\text{C}$ stepwise on SrTiO₃ (001) and performed *in situ* XPS after each deposition step.

Contrary to the thermodynamic prediction, we observe Eu $3d_{5/2}$ spectra dominated by the Eu²⁺ valence, which is associated with EuO in Fig. 2(b). Indeed, only the first interfacial layer forms as Eu₂O₃. For consecutive growth of further layers, the oxygen supply obviously is sufficiently limited, which enables an epitaxial growth of stoichiometric EuO on SrTiO₃.

We argue that this mechanism is due to the limited oxygen mobility of the interface—once an initial layer of the Eu₂O₃ rich phase is formed. This ultrathin intralayer seems to effectively hinder the oxygen supply from the SrTiO₃ substrate. The oxygen conductivity of the SrTiO₃ substrate is, however, strongly dependent on temperature: At room temperature, SrTiO₃ shows very limited oxygen mobility as the EuO/STO interface forms a two-dimensional electron gas (2DEG) as a result of the local oxygen depletion from SrTiO₃ to EuO.¹⁷ Performing higher temperature studies (at and above 700°C), we were able to show only highly oxidized Eu₂O₃ forms. Obviously, the oxygen mobility now exceeds a critical value, and both film and SrTiO₃ serve as a permanent source of oxygen for EuO oxidation. This tunability of interfacial oxygen supply enables performing oxide on oxide growth of two reactive oxides in a well-defined temperature range.

This finding underlines the importance of the oxygen mobility of the film and substrate as active parts of the growth process. Here, we find a temperature-dependent growth window to perform oxide-on-oxide growth of the otherwise reactive oxides EuO and SrTiO₃. The interface may even be used to functionalize the system as 2DEG or as a tunnel barrier, depending on the type of oxygen vacancies formed in SrTiO₃ by the redox process at low temperatures without oxygen replenishing. On the methodical side, the alternating Eu deposition and XPS analysis enable an extensive pre-characterization prior to synchrotron measurements, e.g., unveiling aforementioned two-dimensional electron gas. Moreover, it highlights the usefulness of a combined lab XPS/MBE infrastructure for the characterization of challenging the synthesis of metastable oxide-on-oxide materials.

C. EuO/ITO: An instable oxygen source and sink

What happens eventually if metastable EuO is to be stabilized on an oxide template, which itself is a very good oxygen ion conductor? A suitable substrate to investigate this aspect is ITO/YSZ, i.e., a “virtual substrate” for which an indium tin oxide (ITO) layer is grown sufficiently thick on lattice-matched YSZ (001) such that the YSZ substrate can be disregarded. The growth is performed by reactive MBE at 400 °C using a Eu flux rate of 0.13 Å s⁻¹ and an oxygen partial pressure of 1.7×10⁻⁷ mbar. A 10 nm Al capping is applied after growth to prevent further oxidation.

In order to enable a nondestructive chemical depth-profiling of the EuO film and interface, we here employ hard x-ray photoelectron spectroscopy using variable synchrotron radiation. The HAXPES experiments were conducted at the KMC-1 beamline at BESSY II (Berlin) with the HIKE endstation.²⁵ We vary the inelastic mean free path λ of the emitted photoelectrons as function of the photon energy between 3 (2010) and 9 nm (5000 eV).²⁶

The results are shown in Fig. 2(c). We study the Eu 3d_{5/2} core-level and normalize the data to the binding energy of Eu³⁺. In doing so, we observe a chemical gradient with a small content of Eu²⁺ at the interface, which increases toward the surface. Using established models,²⁷ we identify this as a mixed- or bilayer system with 1.2 nm of EuO and the rest of the nominally 4 nm layer consisting of Eu₂O₃. The thermodynamic Ellingham analysis clearly reveals that EuO on ITO is an unstable phase, unlike YSZ, which is expected to be compatible with EuO growth. We note that at these temperatures, oxygen is extremely mobile in ITO; for samples grown at room temperature, fully reduced In metal is observed at the substrate’s surface (not shown). In this way, HAXPES enables nondestructive chemical depth profiling by varying the probing depth across interfaces and quantifying the different chemical states of the exemplarily highly reactive EuO/ITO interface.

D. Opportunities of redox-assisted oxide growth

The interface-sensitive studies performed by lab XPS and HAXPES show that even on commonly used model substrates like YSZ, which is, e.g., regarded as inert with respect to the formation of Eu³⁺, interfacial redox processes have to be taken into account. Figure 3 summarizes the acquired results, contrasting in (a) the thermodynamical expectations with (b) the spectroscopically acquired results on interface formation of ultrathin film deposition

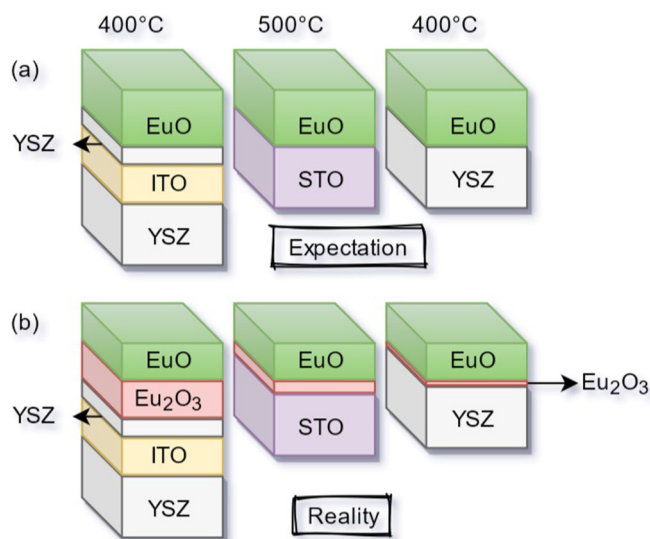


FIG. 3. Schematic depiction comparing the (a) thermodynamic expectation and (b) the experimental findings for interface formation of ultrathin film deposition of EuO on oxides substrates, i.e., ITO, SrTiO₃, and YSZ.

of EuO on (001)-oriented ITO, STO and YSZ substrates, respectively.

Redox-driven interface reactions need to be considered for stabilizing EuO or other metastable materials on any oxide substrate. As summarized in Fig. 4, we performed a study on the growth of EuO onto different oxide substrates, i.e., SrO (5 nm on SrTiO₃), YSZ, LAO, MgO, and LSAT. We find that the substrate’s oxygen ion conductivity correlates well with the film thickness after 5 min of Eu deposition. We could show that the Eu distillation condition can be fulfilled on all of these oxides, rendering them eligible for a kinetic (external) oxygen-free growth mode as described for SrTiO₃.²⁸

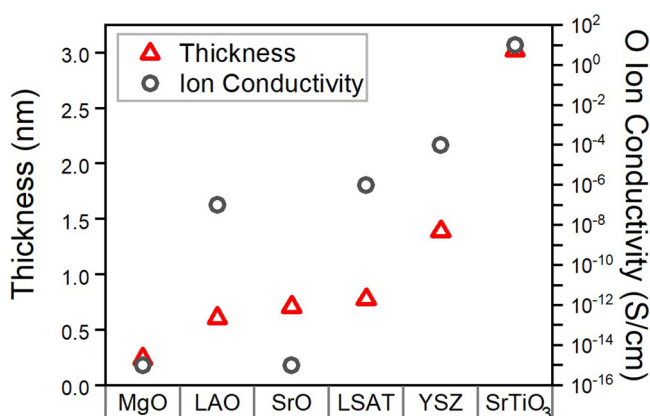


FIG. 4. Correlation of oxygen ion conductivity of selected oxide substrates and redox-grown Eu oxide film thicknesses.

This interface-sensitive study performed by lab XPS shows that even on the commonly used model substrate YSZ, which is regarded as inert with respect to the formation of Eu^{3+} , interfacial redox processes have to be taken into account. This circumstance has to be considered for growing EuO or other metastable materials on any oxide substrate and may even be used as a route to stabilizing oxide phases otherwise not accessible by the standard phase diagram.

III. THERMAL PHASE CONTROL OF OXIDE INTERFACES

Albeit being a classical—if not the most ancient—magnetic material, current research on iron oxide Fe_xO_y thin films actively continues developing due to its applications in a broad range of fundamental and technological fields.⁵ Functional properties of binary iron oxides thereby range from insulators to conductors and from ferromagnets to antiferromagnets.⁷ The prospect of a controlled interconversion between different iron oxide phases, and hence, the deliberate setting of magnetic and/or electrical properties, may open up novel possibilities in oxide electronics. One route toward such tailored reduction-oxidation reactions is by employing an oxide substrate as a - thermally controllable—source or sink of oxygen.

In the following, we will discuss mechanisms that enforce the reduction of magnetite Fe_3O_4 thin films toward lower oxidations states and finally toward Fe metal. Using the depth- and elemental sensitivity of HAXPES allows us to explore the thermally induced chemical transitions between different phases of iron oxide thin films. The information depth for samples illuminated by hard x rays at a photon energy of 4 keV is approximately 20–25 nm, which enables to capture spectroscopic information from the bulk as well as the buried oxide interfaces. All data presented in this chapter was recorded at the HIKE beamline at BESSY II (HZB Berlin, Germany) using a photon energy of 4 keV.²⁵

To introduce the relevant material properties, magnetite Fe_3O_4 crystallizes in an inverse spinel structure with Fe^{3+} occupying the octahedral site, whereas the tetrahedral sites are comprised of a mixture of Fe^{2+} and Fe^{3+} cations. The structure orders magnetically at a Curie temperature of $T_C = 860$ K. Fe_3O_4 has half-metallic conducting properties and undergoes a metal-to-insulator (“Verwey”) transition at $T_V = 120$ K, which is recognized as a sensitive fingerprint for the Fe_3O_4 phase stoichiometry. Details on the growth of Fe_3O_4 films on SrTiO_3 (001) and YSZ(001) substrates by pulsed laser deposition (PLD), as well as their throughout structural and magnetic characterization have been published elsewhere.^{29–31}

A. As-prepared Fe/STO: The unexpected interface

The first challenge is to conclude on the stoichiometry of as-grown Fe_3O_4 thin films. Here, the Verwey transition can serve as a very sensitive signature of the $\text{Fe}_{3-\delta}\text{O}_4$ phase because it can only be detected for $\delta < 0.045$.³² This upper oxygen detection limit may even be more sensitive than a quantitative stoichiometry analysis by XPS or HAXPES, for which the elemental sensitivity is typically in the order of 1% depending on specific core-level cross section and peak intensity. We note that besides the oxygen content itself, also the structural phase, lattice strain, and domain size can alter the Verwey transition temperature of $\text{Fe}_{3-\delta}\text{O}_4$. However, we recently demonstrated that the Fe_3O_4 thin films grow structurally fully relaxed.^{33,34} This is why we can directly relate the observation

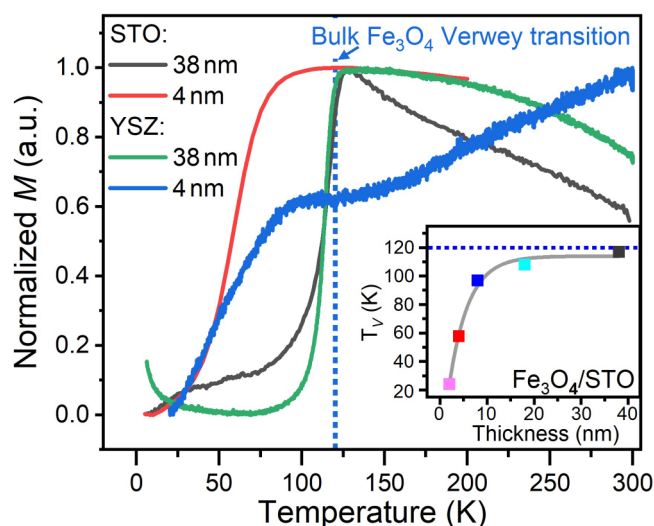


FIG. 5. Magnetization vs temperature $M(T)$ curves to detect Verwey transition of 38 and 4 nm Fe_3O_4 thin films grown on YSZ and SrTiO_3 substrates, respectively. (Inset) Verwey transition temperature T_V as a function of film thickness for Fe_3O_4 grown on SrTiO_3 .

of the Verwey transition to the upper oxygen content, which serves as an alternative measure in addition to HAXPES data.

The Verwey transition was recorded for Fe_3O_4 thin films grown on YSZ and SrTiO_3 with thicknesses of 38 and 4 nm via magnetization vs temperature $M(T)$ curves, as shown in Figure 5. Below T_V , Fe_3O_4 transfers from a cubic to a monoclinic structure, which causes a decrease of the magnetization. The magnetization as a function of temperature $M(T)$ of the 38 nm films grown on both YSZ and SrTiO_3 drops around 120 K, which is corresponding to the Verwey transition. This observation suggests a bulklike stoichiometry of the 38 nm Fe_3O_4 films grown on both SrTiO_3 and YSZ.

For an ultrathin film of 4 nm thickness grown on YSZ and SrTiO_3 , the Verwey transition is still detectable but decreases to 60 K, as shown in the inset of Fig. 5. While its detectability indicates a high structural and stoichiometric quality of the Fe_3O_4 films, the reduced T_V points toward its reduced dimensionality. Indeed, by HAXPES analysis of the Fe 2p spectra, we can extract the formation of a 2 u.c. of the $\gamma\text{-Fe}_2\text{O}_3$ intralayer between Fe_3O_4 and the substrates,^{29,30} which reduces the effective Fe_3O_4 thickness. From a thermodynamic perspective, this finding is unexpected as no driving force for further oxidation of Fe_3O_4 shall exist according to an Ellingham analysis—at least for bulk Fe_3O_4 and substrates. Once more, we find an oxide interface behaving opposite to theoretical predictions—which, in turn, opens up novel possibilities for its thermal tunability via the substrate’s oxygen supply, which we explore in the following.

B. Tuning iron oxide phases by postannealing

To record the thermally induced phase transition from Fe_3O_4 , HAXPES experiment on the above samples were conducted in the

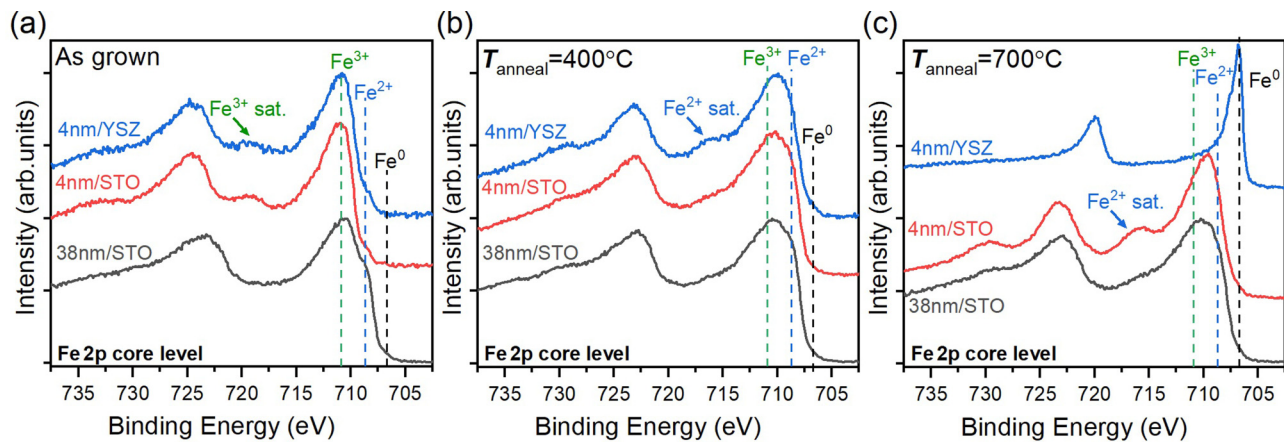


FIG. 6. Fe 2p core level spectra recorded for 38 nm and 4 nm Fe_3O_4 films grown on SrTiO_3 and YSZ. (a) As-grown Fe_3O_4 films, (b) Fe_3O_4 films annealed at temperatures of $T = 400^\circ\text{C}$ and (c) $T = 700^\circ\text{C}$ in UHV atmosphere, respectively.

following manner: Fe 2p core-level spectra were recorded during stepwise postannealing of the samples between temperatures of 25–700 °C in UHV, and each step was stabilized for 20 min. Moreover, to test whether the Fe 2p spectra are recorded at quasiequilibrium, a film of 4 nm was annealed at 600 °C for 90 min, and HAXPES Fe 2p was recorded every 30 min. No changes in peak position or -shape appear in the spectra.

Figure 6(a) depicts Fe 2p core-level spectra of the as-grown Fe_3O_4 films. To identify the Fe valency, the experimental spectra were compared to reference data of FeO ,³⁵ Fe_2O_3 , and Fe_3O_4 .³⁶ The emergence and position of satellite peaks yield clear indication for the presence of Fe^{3+} and/or Fe^{2+} , see Fig. 6(a). The satellite peaks of FeO and Fe_2O_3 phases have binding energies E_B of 715.5 and 719 eV, respectively. On the other hand, the satellite peaks of Fe_3O_4 , which has a mixed oxidation state of Fe^{2+} and Fe^{3+} , merge and thus disappear, as apparent for the 38 nm film grown on SrTiO_3 substrate in Fig. 6(a). For 38 nm thick Fe_3O_4 , consequently, we find that the two satellites are merged. Moreover, the $\text{Fe } 2p_{3/2}$ core level is composed of the Fe^{3+} peak and a shoulder that refers to Fe^{2+} . We conclude on a bulklike stoichiometry of 38 nm thick Fe_3O_4 films. For 4 nm films grown on SrTiO_3 and YSZ substrates, we observe that the Fe^{3+} satellite peak appears accompanied by a decrease Fe^{2+} peak shoulder at the $\text{Fe } 2p_{3/2}$ peak. Both observations suggest the formation of an interfacial Fe_2O_3 phase in addition to Fe_3O_4 .

For films annealed at $T_{\text{anneal}} = 400^\circ\text{C}$ in UHV-atmosphere, as shown in Fig. 6(b), the films with thicknesses of 4 nm and 38 nm grown on STO substrates show the appearance of a satellite peak at $E_B = 715.5\text{ eV}$, which indicates the formation of a FeO and partial Fe_3O_4 phase. However, for film grown on YSZ, the satellite peak intensity at $E_B = 715.5\text{ eV}$ is stronger and indicates the full reduction to FeO . On the other hand, for films annealed at $T_{\text{anneal}} = 700^\circ\text{C}$ in UHV-atmosphere as shown in Fig. 6(c), the 38 nm film grown on STO shows a partial reduction to FeO , whereas the 4 nm film grown on STO shows a full reduction to FeO indicated by the intensities of the satellite peaks. Surprisingly, the 4 nm thick film grown on YSZ is fully reduced to Fe metal.

C. Beyond the standard phase diagram: A thermodynamic discussion

The previous results unveil the strong differences between YSZ and STO substrates in their affinity to be chemically reduced. However, the formation of interfacial $\gamma\text{-Fe}_2\text{O}_3$ is observed for both systems, $\text{Fe}_3\text{O}_4/\text{STO}$ and $\text{Fe}_3\text{O}_4/\text{YSZ}$. Figure 7 summarizes the resulting heterosystem before and after annealing. The mechanism for the formation of the interfacial $\gamma\text{-Fe}_2\text{O}_3$ phase between Fe_3O_4 films and STO and YSZ substrates remains to be discussed.

Taking into account the thermodynamic properties of all constituents, SrTiO_3 has a lower Gibbs free energy of formation $\Delta G_F^\circ = -1588.4\text{ kJ/mol}$ compared to Fe_3O_4 ($\Delta G_F^\circ = -1015.4\text{ kJ/mol}$). Therefore, STO is not expected to oxidize Fe_3O_4 . However, oxygen vacancies perturb the formation energy for TiO_2 -terminated STO to 461.5 kJ/mol.

Consequently, the formation of an oxidized $\gamma\text{-Fe}_2\text{O}_3$ intralayer may be explained by the oxygen diffusion from the STO substrate due to the reduced surface formation energy by oxygen vacancies of TiO_2 -terminated STO surfaces, which enables the migration of oxygen from STO into Fe_3O_4 . We note that this mechanism may simultaneously lead to the formation of reduced Ti^{3+} at the STO interface, which is the key prerequisite for the formation of a redox 2DES.¹⁷

From bulk thermodynamics, the formation enthalpies of Fe_3O_4 and YSZ have similar values. Therefore, no clear expectation of which phase may reduce the other can be drawn. It should be noted, however, that since YSZ is such a good oxygen ion conductor, any formation of additional oxygen vacancies (concomitant with reduction of Zr) at the interface will be followed by a rapid redistribution, making the concentration of excess oxygen vacancies at the interface quite small.

Additionally, YSZ is known to be a good electrolyte because of its high oxygen conductivity, which is influenced by the doping level as well. Therefore, oxygen can diffuse from the outer atmosphere through the YSZ substrate and cause the formation of an

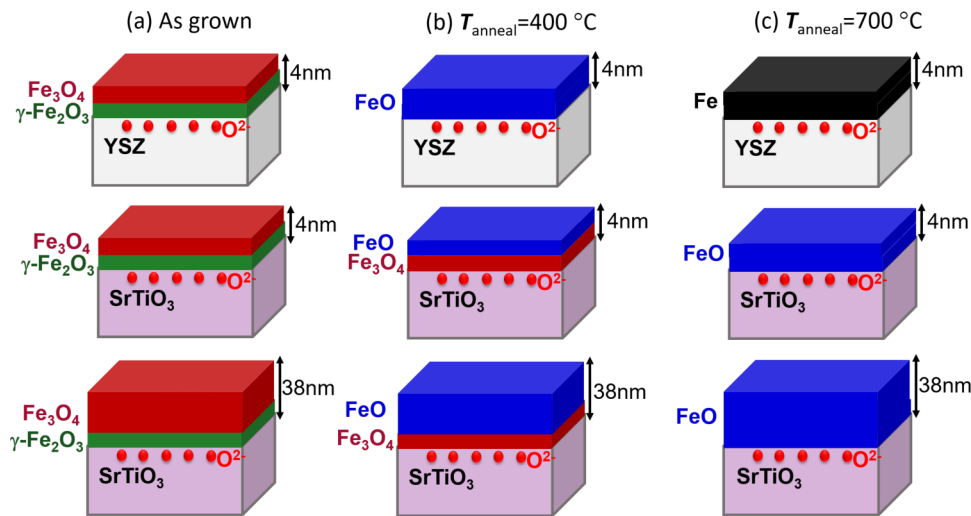


FIG. 7. (a) Schematics of as-grown iron oxide heterostructures with thicknesses of $d = 4\text{nm}$ (50 % $\gamma\text{-Fe}_2\text{O}_3$ and 50 % Fe_3O_4) on YSZ (top) and Nb:SrTiO₃ substrates (middle), respectively, and $d = 38\text{nm}$ on Nb:SrTiO₃ (bottom). (b) and (c) The same set of samples but annealed to (b) $T_{\text{anneal}} = 400^\circ\text{C}$ and (c) $T_{\text{anneal}} = 700^\circ\text{C}$ in UHV-atmosphere.

Fe_2O_3 intralayer. Therefore, the oxygen conductivity of YSZ is a key factor for the formation of an oxidized Fe_3O_4 intralayer. However, the perturbation of oxygen vacancy concentration caused by this redistribution within the substrate crystal plays a negligible role.

To conclude, we studied the effect of annealing in different oxygen pressure and the emerging redox processes of Fe_3O_4 interfaces. A thermodynamics modeling allows to understand phase transformations between Fe_3O_4 , $\gamma\text{-Fe}_2\text{O}_3$, and FeO through the oxygen migration across interfaces with oxide substrates SrTiO₃ and YSZ. This finding convincingly demonstrates the important role of the oxide substrates STO and YSZ as oxygen scavengers or suppliers. In this way, alternative opportunities emerge to control interface and thin-film functionalities of all-oxide heterostructures.

IV. BAND ALIGNMENT AT OXIDE INTERFACES

Key parameters of any semiconductor (SC) device are the electronic band alignment and -offsets at the interfaces of a metal-insulator (M/I) heterostructure. HAXPES can serve as an experimental tool to directly extract the valence band (VB) offsets of buried interfaces.¹¹ In addition, also the interfacial chemical state is accessible, which makes HAXPES a unique tool for a thorough interface characterization.⁹ Furthermore, performing HAXPES experiments *in operando*, i.e., under applied bias voltage, both the band alignment and the chemical state of a M/I device can be determined under realistic operation conditions—and captured in a concurrent measurement.^{37,38} In this chapter, we discuss an Au/NiFe₂O₄/SrTiO₃ heterostructure as a prototype example for an *in operando* HAXPES experiment, as schematically sketched in Fig. 8.

NiFe₂O₄ directly compares to Fe_3O_4 , as both materials adopt the inverse spinel crystal structure. In NiFe₂O₄, divalent Ni cations occupy the Fe^{2+} lattice sites of the Fe_3O_4 unit cell. The thereby altered magnetic exchange and electronic correlations turn NiFe₂O₄ into an (also) ferrimagnetic but insulating material, with a similar

Curie temperature of about 850 K.³⁹ In Fig. 9(b), the NiFe₂O₄ spectral signatures of the Fe 2p core level spectra thus shows a Fe^{3+} -only feature which lacks the Fe^{2+} shoulder, as observed for Fe_3O_4 in Fig. 6(a). With regard to the chemical stability, however, NiFe₂O₄ and Fe_3O_4 strongly differ: the NiFe₂O₄/STO interface turns out to be chemically extremely robust compared to Fe_3O_4 /STO. No signatures of interfacial redox reactions could be observed by HAXPES for NiFe₂O₄.⁴⁰ Thus, the NiFe₂O₄/STO heterostructure serves as a prototype example for a quasi-nonreactive M/I interface, which, in turn, is a prerequisite for an *in operando* HAXPES characterization.

A. Experimental *in operando* HAXPES

The design of samples for *in operando* HAXPES measurements requires metal top electrodes to apply a bias voltage. On the

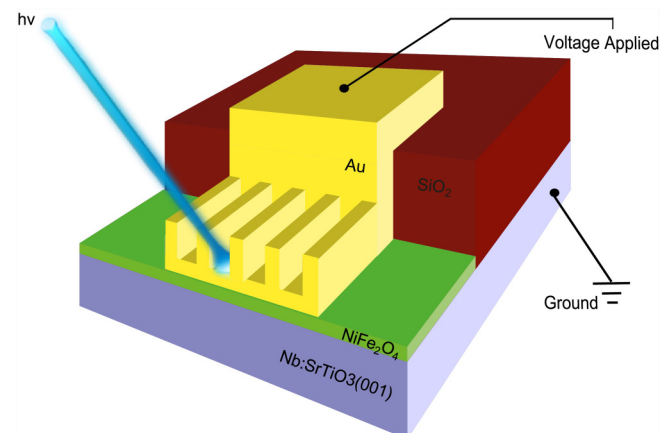


FIG. 8. Schematics of an *in operando* HAXPES measurement on a structured Au/NiFe₂O₄/SrTiO₃ heterostructure.

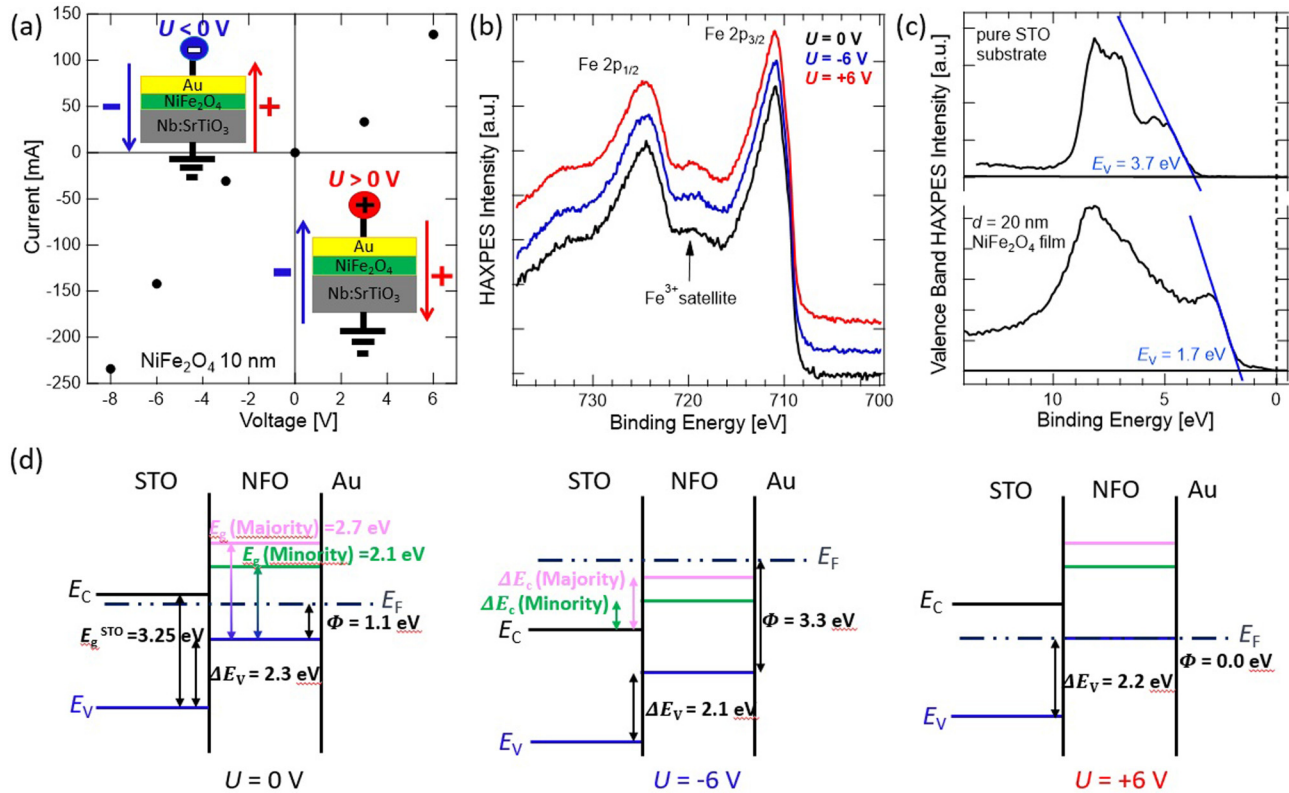


FIG. 9. (a) Electric I - V curves recorded during *in operando* HAXPES of a Au/NiFe₂O₄/SrTiO₃ heterostructure. (b) BE-corrected Fe 2p core levels, for which the on-potential spectra under ± 6 V bias are shifted on top of the 0 V measurement. (c) Determination of the valence band offset of the reference SrTiO₃ and NiFe₂O₄ samples. (d) Band alignment determined by the Kraut method with respect to the applied voltage.

other hand (in order to adapt to the information depth of the HAXPES experiment), these electrodes need to be structured into different regions which either can be electrically contacted (thick metal pad) or can be probed by HAXPES while applying the bias potential (thin metal overlayer).

Figure 8 sketches a possible heterostructure for *in operando* HAXPES. Half of the Nb-doped SrTiO₃ substrate is covered with a 500 μm SiO₂ film, which serves as a buffer between the STO back electrode and Au top electrode. On top of STO, a 10 nm NiFe₂O₄ layer is deposited via pulsed laser deposition. Next, a 4 nm thin Au pad (2 × 3.6 mm²) is deposited *ex situ* via electron beam vapor deposition, which overlaps the SiO₂ and NiFe₂O₄/SrTiO₃ areas. On top of this thin gold pad, a 40 nm gold finger structure is deposited. The fingers width and distance between the fingers is 0.2 mm, respectively. The top Au electrode is connected to the voltage source and the SrTiO₃ substrate is grounded.

In operando HAXPES experiments were performed at beamline P09 (now P22) at PETRA III (DESY Hamburg, Germany)⁴¹ in normal emission geometry using a photon energy of 6 keV. For each voltage step, the electrical current was measured, see Fig. 9(a). As reference data, spectra of a SrTiO₃ substrate, a 20 nm NiFe₂O₄ film and a 50 nm Au film were recorded.

B. Chemical stability of the NiFe₂O₄/STO interface

In order to determine the band alignment of the Au/NiFe₂O₄/SrTiO₃ heterostructure *in operando*, the layers and interfaces need to be chemically stable—not only thermodynamically but also under applied bias voltages during the HAXPES measurement.¹³ Figure 9(b) displays the Fe 2p core level for varying applied voltages, whereby the on-potential spectra had been shifted on the binding energy (BE) scale on the zero voltage Fe 2p position. No spectral changes of the core levels are observed. In particular, at the low binding energy flank of the Fe 2p_{3/2} peak, no shoulder of a possibly emerging Fe²⁺ component can be identified, and also the position of the Fe³⁺ satellite peak remains unchanged. Hence, NiFe₂O₄ can be assumed to be chemically stable during the *in operando* HAXPES measurement.

For each voltage step, the electrical current was observed to check whether the sample had not been shorted. A positive applied voltage refers to a direction where negative charges move from SrTiO₃ to NiFe₂O₄, while a negative applied voltage refers to a direction vice versa. The resulting I - V curve is shown in Fig. 9(a). We find a symmetrical and nonohmic response indicative of a M/SC/M structure. Although NiFe₂O₄ is expected to be insulating,

the growth of NiFe_2O_4 on SrTiO_3 introduces defects like dislocations or mosaicity due to the large lattice strain.^{39,40} NiFe_2O_4 , therefore, electrically acts as a semiconductor. In general, throughout the entire *in operando* HAXPES measurement process, the sample was electrically and chemically stable, as shown in Figs. 9(a) and 9(b).

C. Band alignment analysis via HAXPES

In a simple but powerful model used in semiconductor physics, the valence band (VB) offset ΔE_v at the interface of two SCs A and B is simply determined by the energy difference of their VB maxima E_v , $\Delta E_v = E_v^A - E_v^B$. The same relation holds for the Schottky barrier height Φ_B of a metal/SC interface; here, the metal valence band maximum is given by the Fermi energy, $\Phi_B = E_F^M - E_v^{SC}$.

In an (oxide) heterostructure, however, the VBs of the different materials are overlapping and thus the VBs of the individual layer often cannot be directly recorded by HAXPES. Therefore, an indirect method is typically applied, which relates a core level binding energy position to the actual position of the valence band. This so-called "Kraut model" assumes flatbands and chemically stable interfaces.¹³ If these conditions are fulfilled, it can be used to determine the band alignment and the band offset at the interfaces of (oxide) heterostructures, here $\text{Au/NiFe}_2\text{O}_4/\text{SrTiO}_3$.

According to Kraut's model,¹³ the measured energy difference between any core level peak maximum and the VB maximum of a reference material A is taken as a constant value, also if material A is part of a heterostructure. Thus, binding energy changes of the core level should directly reflect the same changes at the VB maximum,

$$(E_{cl}^A)_{ref} - (E_v^A)_{ref} = (E_{cl}^A)_{het} - (E_v^A)_{het}. \quad (1)$$

Due to the element selectivity of HAXPES, specific core levels can be related to the individual layers of a heterostructure and hence the VB position of the individual layers can be determined. The experimentally not accessible valence band maximum $(E_v^A)_{het}$ is now substituted by the difference of the equivalent core level binding energies relative to the reference sample,

$$(E_v^A)_{het} = (E_v^A)_{ref} - [(E_{cl}^A)_{ref} - (E_{cl}^A)_{het}]. \quad (2)$$

Now, the VB offset E_v or Schottky barrier height Φ_B between different materials A and B, here $\text{Au/NiFe}_2\text{O}_4$ and $\text{NiFe}_2\text{O}_4/\text{SrTiO}_3$, becomes experimentally accessible by using Eq. (2).

For the determination of the band alignment of the $\text{Au/NiFe}_2\text{O}_4/\text{SrTiO}_3$ model sample, the core level binding energies of the Au $4f_{7/2}$ level for the Au top electrode, the Fe $2p_{3/2}$ and Ni $2p_{3/2}$ level for NiFe_2O_4 , and the Ti $2p_{3/2}$ and Sr $3d_{5/2}$ levels for the SrTiO_3 layer are analyzed. As reference samples an uncovered SrTiO_3 substrate, a 20 nm NiFe_2O_4 film and a 50 nm Au film are used. The Fermi level E_f of Au was used as binding energy reference and set to zero. As depicted in Fig. 9(c), the VB edges E_v of the SrTiO_3 and NiFe_2O_4 reference samples are determined by fitting.⁴²

In Fig. 9(d), the resulting band alignment is shown. The conduction band positions E_c are calculated by adding the bandgap E_g

to the VB offsets ΔE_v . For SrTiO_3 , a bandgap of $E_g = 3.25$ eV is assumed⁴³ and for NiFe_2O_4 the calculated majority and minority, bandgaps of $E_g = 2.7$ eV and $E_g = 2.3$ eV are used.⁴⁴ The bias dependent band alignments diagrams for $U = 0$ V, 6 V, -6 V of the $\text{Au/NiFe}_2\text{O}_4/\text{SrTiO}_3$ heterostructure are shown in Fig. 9(d), with the corresponding I - V curve depicted in Fig. 9(a).

We find the spectroscopically determined ΔE_v at the $\text{NiFe}_2\text{O}_4/\text{SrTiO}_3$ interface being independent of the applied voltage, while Φ_B at the $\text{Au/NiFe}_2\text{O}_4$ interface strongly changes. Thus, the electrical transport characteristics of the $\text{Au/NiFe}_2\text{O}_4/\text{SrTiO}_3$ heterostructure are mainly governed by the $\text{Au/NiFe}_2\text{O}_4$ interface. For $U = 0$ V, the Fermi level E_f is located in the bandgap of NiFe_2O_4 and close to the conduction band E_v of SrTiO_3 . Due to its Nb-doping, SrTiO_3 is electrically conducting. For small voltages, NiFe_2O_4 acts as a barrier, and only small currents are expected, which fits well with the observed nonohmic, symmetrical I - V curve in Fig. 9(a). At $U = -6$ V, the Fermi level E_f is located in the conduction band of NiFe_2O_4 and SrTiO_3 . Thus, there is a conducting path established, which is also observed in the I - V curve. In the case of $U = 6$ V, the Fermi level E_f aligns with the valence band edge of NiFe_2O_4 and lays in the bandgap of SrTiO_3 . Thus, again a conducting channel is established, which is confirmed by the I - V curve in Fig. 9(a).

From the above experiments, an element-specific quantification of band alignments of a complex oxide heterostructure was realized, which confirms the results of electrical I - V measurements. In that, *in operando* HAXPES is a powerful spectroscopic tool to probe multilayer devices under realistic operation conditions.

V. INTERFACE OXIDE EXCHANGE IN FERROELECTRIC CAPACITORS

Sections II and III discussed mechanisms by which controlled oxygen supply by oxide substrates can be utilized to deliberately set ferro(i)magnetic oxide properties of ultrathin films. On the other hand, ferroelectricity in dielectric HfO_2 -based compounds is mainly introduced by the *absence* of oxygen, introduced either by doping or directly by oxygen vacancies.⁴⁵ Ferroelectric (FE) capacitors based on simple metal-FE insulator-metal (MIM) structures are envisioned as efficient nonvolatile memory devices.⁴⁶ Since its discovery around 2010, HfO_2 -based ferroelectric materials, in particular, $\text{Hf}_{0.5}\text{Zr}_{0.5}\text{O}_2$ (HZO), emerged as most promising candidates due to their outstanding CMOS compatibility.

In practice, however, performance instabilities, such as the so-called wake-up, imprint, and fatigue effects, are still poorly controllable and currently hamper its application in commercial FE memory devices.^{47,48} The common feature of these issues is the emergence of excess oxygen vacancy defects located within the ferroelectric HfO_2 -based layer with an increased density at the electrode interfaces. Thus, the control of the oxygen defect density within the HfO_2 -based layer and at its interfaces is currently of major interest.

It has become evident that the choice of the metallic electrode material in MIM capacitors plays a crucial role, in particular, because the interface chemical state modulates the oxygen exchange across the interface—which can either act passively or rather as a source or sink of oxygen. Hence, the material choice can either increase or reduce the defect density at the HfO_2 interface and

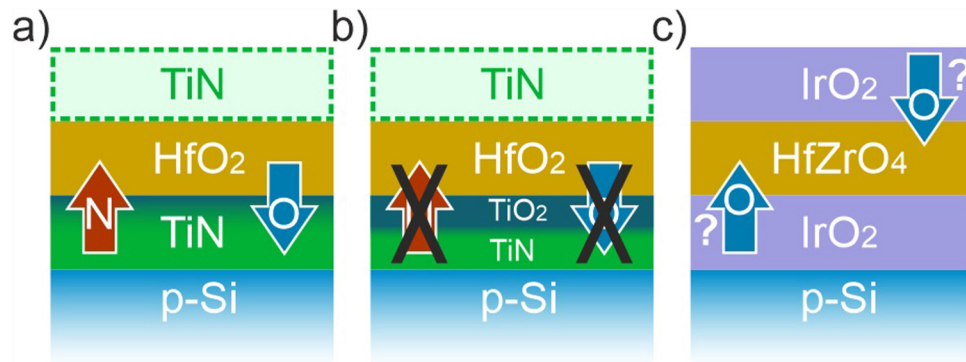


FIG. 10. Different interface oxygen exchange mechanisms occur in HfO₂-based MIM structures, dependent on the choice of the metal electrodes: (a) oxygen scavenging by a TiN electrode, (b) interface passivation by a TiO₂ interlayer, and (c) possible oxygen supply by an IrO₂ electrode.

exploiting the tunability of oxygen vacancy density is a major aspect in current MIM design. HAXPES as an element-selective, depth-sensitive, and nondestructive analysis tool serves as an ideal probe for the emerging interface chemistry. All HAXPES data presented in this section had been recorded at the beamline P22 of PETRA III (DESY Hamburg, Germany) using a photon energy of 6 keV.⁴⁹

Figures 10(a)–10(c) schematically depicts three MIM structures for which oxygen exchange mechanisms across the interface was explored by HAXPES. Their specific preparation conditions by either physical vapor deposition (PVD)⁴⁵ or/and atomic layer deposition (ALD)⁵⁰ were taken into account for discussion of the spectroscopic results, as, in particular, the oxygen supply before or during HfO₂ layer growth significantly alters the interface properties. Moreover, all three capacitors devices had been characterized electrically by polarization-voltage (P-V) curves,^{45,51} and hence a direct relation between the interface chemical properties and ferroelectric state of the MIM structures can be drawn.

A. Oxygen scavenging by TiN electrodes

For TiN/HfO₂/TiN capacitors, the interface properties strongly depend on the specific PVD growth parameters: Fig. 11 depicts the Hf 4f core levels recorded from two samples for which either no or 2 SCCM gaseous oxygen was provided before and during the HfO₂ layer growth. For a direct comparison, the rigid binding energy shift between the two measurements was corrected, and both spectra were subtracted from each other. This differential spectrum (shaded blue area) reveals a double peak structure with the same energy splitting as the Hf 4f doublet but shifted by 600 meV to lower BE values and with an intensity ratio of about 5% compared to the main Hf 4f doublet. This feature is assigned to a spectral contribution of a Hf³⁺ valency in agreement with the literature,⁵² and its intensity strongly decreases with the amount of supplied oxygen during the growth process as discussed in Ref. 53. We note that the N 2s component, which appears at about 15.5 eV binding energy, can be neglected in the spectral analysis of the Hf 4f level. Compared to Hf 4f and N 1s core levels, the N 2s peak

has an about 1 order of magnitude lower cross section and is covered by a 10 nm HfO₂ layer, hence, its intensity is below the detection limit.

For the N 1s core level shown in the inset of Fig. 11, we also compared the differential spectra and found an enhanced spectral weight at the lower binding energy side for the sample without additional oxygen supply. This contribution can be assigned to the presence of HfN.⁵⁴ Further, the peak located at $E_B = 397.5$ eV is assigned to TiN and the peak fit at $E_B = 396.7$ eV can be related to TiN_xO_y contributions.⁵⁵ In analogy to the Hf 4f spectrum, the formation of the HfN related component is found to decrease the amount of oxygen provided during the growth process.⁵³

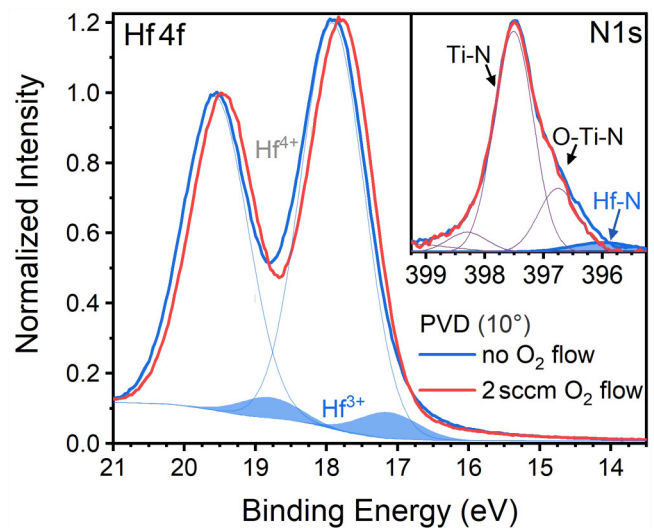


FIG. 11. Hf 4f core-level spectra for TiN/HfO₂/TiN capacitors grown at different oxygen ambiances (0 and 2 SCCM). Without additional oxygen supply, a Hf³⁺ component appears (shaded area). The inset shows the related N 1s spectra, for which a HfN component is evident.

The emergence of Hf^{3+} spectral weight in the Hf 4f core level may either be interpreted as HfN contribution or as an indirect signature of positively single and double-charged oxygen vacancies, V^\bullet and $\text{V}^{\bullet\bullet}$. From angular dependent HAXPES measurements (not shown), the Hf^{3+} contribution can be located at the interface between HfO_2 and the bottom TiN electrode. As the HfN component is observed in the N 1s core-level spectra, an interfacial HfN formation seems likely. However, oxygen vacancies are also known to be enhanced at the interfaces. Thus, both contributions may contribute to the Hf^{3+} component.

At this point, we conclude that without additional oxygen supplied during the PVD growth, the TiN electrode can exchange nitrogen and oxygen with the HfO_2 layer during the rapid thermal annealing process, which results in the formation of a TiO_x/HfN interface layer, as schematically depicted in Fig. 10(a). The incorporation of nitrogen in the HfO_2 may, in turn, change the vacancy features at the interface as discussed by Baumgarten *et al.*⁵⁶

B. Interface stabilization

What happens at the TiN/ HfO_2 bottom interface if additional oxygen is supplied before and during PVD growth, and what are the consequences for the defect distribution in HfO_2 ? From the previous results, we expect an interface exchange of oxygen and nitrogen dependent on the gradual increase of oxygen dosage.

In Fig. 12, the Ti 2p core level of samples prepared under different oxygen flows reveal contributions of several chemical species, namely, TiN, TiN_xO_y suboxides,^{57,58} and TiO_2 . The increase of the oxygen flow during growth leads to a significant increase of the spectral weight of the TiO_2 component, starting from a small spectral weight at 0 SCCM to a $\sim 1:1$ ratio of TiO_2 and TiN for 2 SCCM. From angular-dependent HAXPES measurements (not shown), it can be concluded that the TiO_2 contribution is located on top of the TiN bottom layer.

Since the TiO_2 peaks already appear for the amorphous HfO_2/TiN system (not shown) and thus are not related to the rapid thermal annealing crystallization process, an oxygen scavenging from HfO_2 can be excluded. Rather we conclude on the formation of a TiO_2 interlayer between the TiN bottom electrode and HfO_2 . The TiO_2 interlayer thickness has been calculated from the TiO_2/TiN intensity ratio, taking into account the reduction of the TiN thickness at the expense of the TiO_2 growth (see Ref. 53 for a detailed description). The resulting self-limiting layer growth is depicted in the inset of Fig. 12.

From the above HAXPES experiments, we propose the following chemical processes, which strongly determine the interface properties of TiN/ HfO_2/TiN capacitors. The oxygen supply before HfO_2 growth generates a TiO_2 interface layer, which is self-limiting at about 3.5 nm. This layer effectively stabilizes the interface and prevents the exchange of oxygen and nitrogen. TiO_2 itself is chemically very stable and thus not expected to supply oxygen to the HfO_2 layer. Moreover, the interface stabilization by a TiO_2 buffer offers the possibility to design the defect properties of the atop HfO_2 layer deliberately by specific growth parameters.

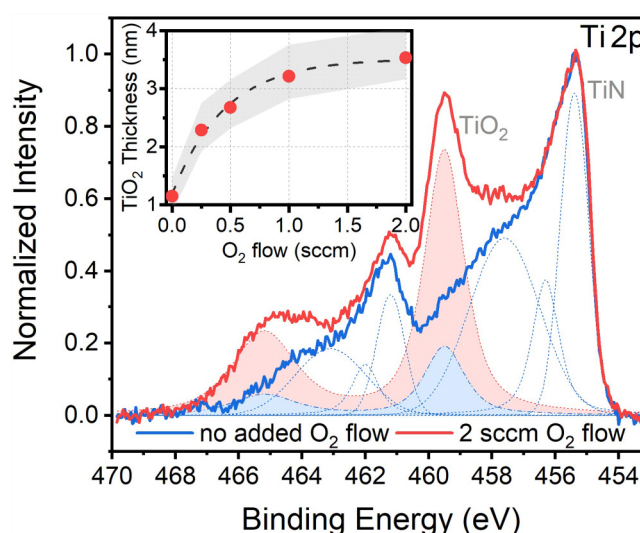


FIG. 12. Ti 2p spectra recorded from the TiN bottom electrode of TiN/ HfO_2 -based MIM structures. A TiO_2 component appears with increasing oxygen supply before and during PVD growth of HfO_2 and signifies an interface oxide layer formation. The inset shows the oxygen flow-dependent thickness of this TiO_2 intralayer.

C. Oxygen supply by IrO_2 electrodes

Finally, we explore the possibility of supplying oxygen into ferroelectric HfO_2 by an adjacent metal electrode. IrO_2 electrodes have been utilized as oxygen supplier in $\text{IrO}_2/\text{PZT}/\text{IrO}_2$ ferroelectric MIM structures.⁵⁹ Due to the resulting option to control the oxygen vacancy concentration in PZT, the ferroelectric performance of such MIM structure could be significantly optimized. The same effect was anticipated for $\text{IrO}_2/\text{Hf}(\text{Zr})\text{O}_2/\text{IrO}_2$ MIM structures by increased controllability of HZO-related defects.

From the chemical perspective, IrO_2 readily supplies oxygen because it is an unstable compound and can be easily reduced to metallic iridium at elevated temperatures.⁵¹ Moreover, the choice of different annealing atmospheres has been found to crucially impact the IrO_2 composition and on the crystallization anneal process.⁶⁰ In Fig. 13, the Ir 4p and the O 1s core-levels are displayed. The Ir 4p emission around 495 eV shows different binding energies for annealing of the $\text{IrO}_2/\text{Hf}(\text{Zr})\text{O}_2/\text{IrO}_2$ in an oxygen atmosphere (OA) compared to forming gas annealing (FGA) (FG: 90% Ar, 10% H_2). The OA Ir 4p_{3/2} level appears at 800 meV higher binding energy, indicating a chemical shift. The IrO_2 top electrode is reduced to metallic Ir by the FG ambient, whereas the oxygen atmosphere, in turn, stabilizes the IrO_2 electrode. In addition, the metallic FGA Ir electrode shows an oxygen content at a binding energy of 533 eV, which is related to oxygen unbound to Ir (see the inset).⁶⁰

The emergence of metallic Ir electrodes containing unbound oxygen is of special interest to control the ferroelectric behaviour of the Ir/HZO interface during electrical switching of the MIM device. In the inset of Fig. 13, two spectra are displayed for which

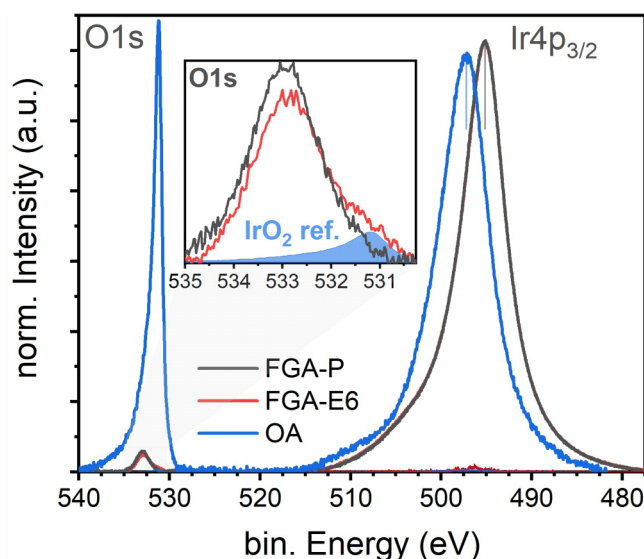


FIG. 13. Ir 4p and O 1s emission of the top electrode. The spectrum shifted to higher binding energy reflects the IrO₂ emission of the OA sample, the spectra on the lower BE side reflect the chemically. FGA-P and FGA-E6 are related to electrically untreated and 10⁶ times electrically cycled samples, respectively. The inset shows the O 1s emission of these two samples.

the FGA-annealed MIM device either had been electrically switched back and forth 10⁶ times (FGA-E6) or is electrically still untreated (FGA-P). A comparison reveals a modification of spectral weight in the O 1s component. The intensity of the unbound oxygen component at 533 eV decreases, while an additional component at 531 eV appears. This emission can be related to IrO₂. Thus, the application of the electrical switching pulses seemingly induces a chemical reaction at the interface. Such a reaction is most likely induced by charge injection into defect states at the interface. Whether this is accompanied by an oxygen migration across the interface cannot be concluded from the current HAXPES results and requires further investigations.

The emergence of the IrO₂ component, as shown in Fig. 13 can be directly related to a changed band alignment at the interface. As discussed in Sec. IV, binding energy shifts of core levels can be used as a measure of the binding energy shifts of the VB maximum relative to the Fermi level.¹³ Here, the Hf 4f binding energy shift is used as a relative measure of the interfacial band alignment. Figure 14 shows the Hf 4f spectra of the OA and FGA samples, compared to samples annealed without top electrode [see Fig. 14(c)]. From the Hf 4f binding energies of the samples without the top electrode, the band alignment at the bottom electrode is deducible. The IrO₂ top electrode of the OA sample shows a small shift of 130 meV toward lower binding energies [Fig. 14(b)], whereas the Ir top electrode of the electrically untreated FGA and FGA-P sample show a shift of 320 meV toward higher binding energies [Fig. 14(a)]. After 10⁶ switching cycles (FGA-E6); however, the Hf 4f level has shifted back to the same binding energy as observed

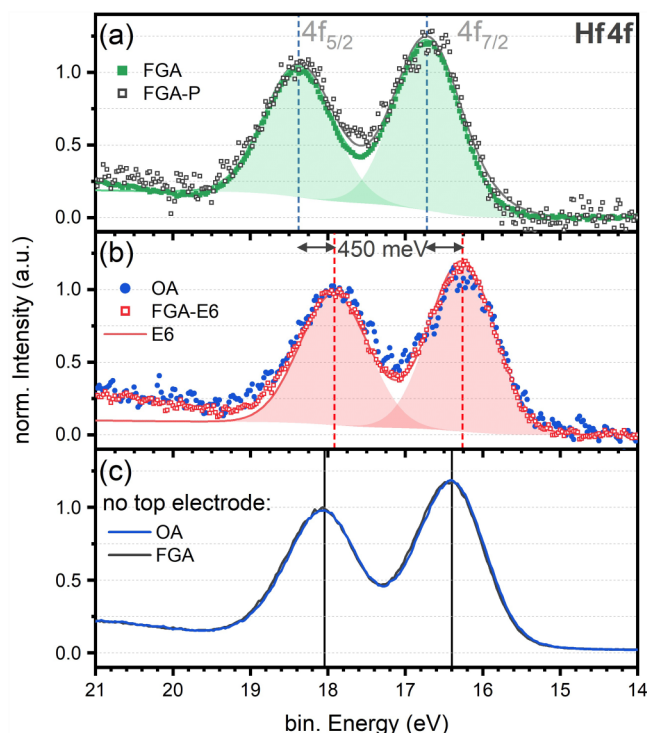


FIG. 14. HAXPES spectra of the Hf 4f core levels for samples (a) and (b) with top electrode under different annealing ambiances and cycling conditions, and (c) annealed without top electrode.

for the IrO₂ OA sample, see Fig. 14(b). This coincides with the appearance of the IrO₂ component at the interface and directly reflects the change from an Ir-related band alignment toward an IrO₂ related one. This shows the strong relation between interface chemistry and band alignment and again highlights the capability of HAXPES to address both.

VI. SUMMARY

In summary, oxide interfaces between (ultra-)thin films and substrates had been shown to offer exciting possibilities to set functionalities deliberately by a controlled oxygen exchange. The element-sensitivity of soft- and hard x-ray photoelectron spectroscopy allows to disentangle the specific mechanisms of how adjacent materials affect each other through, e.g., chemical reactions, ion diffusion, or charge transfer, which may be related to electronic band bending or defect formation. In addition, the depth-sensitivity of HAXPES has been shown to be indispensable to probe these phenomena in a nondestructive manner at hidden interfaces and in real multilayer devices. In this regard, we presented spectroscopic results on emerging interface states and their tunability for selected ferro(i)magnetic and ferroelectric heterostructures—covering fundamental aspects and exploring application-relevant devices. The ability to tailor functional thin film properties will be key for future applications, e.g., in oxide

electronics, which require full control over these complex electronic ground states.

ACKNOWLEDGMENTS

The authors gratefully acknowledge beamtime support by Ch. Schlueter, A. Gloskovski, Y. Matveev, and W. Drube at the HAXPES beamline P22 (PETRA III, DESY Hamburg). Likewise, the authors wish to thank M. Gorgoi and R. F. Duarte for their support at the HIKE beamline (BESSY II, HZB Berlin). The authors acknowledge DESY (Hamburg, Germany), a member of the Helmholtz Association HGF, for the provision of experimental facilities. Funding for the HAXPES instrument at beamline P22 by the Federal Ministry of Education and Research (BMBF) under Contract Nos. 05KS7UM1 and 05K10UMA with Universität Mainz and Nos. 05KS7WW3, 05K10WW1, and 05K13WW1 with Universität Würzburg is gratefully acknowledged. The authors acknowledge R. Dittmann for providing the PLD setup at FZJ as well as O. Petravic and T. Brückel for providing measurement time at VSM at FZJ. T.S., L.B., and M.M. acknowledge valuable discussions with U. Schroeder and T. Mittmann. Funding is acknowledged from the European Union's Horizon 2020 research and innovation programme under Grant Agreement No. 780302. M.H.H. acknowledges support through a Tasso Springer Fellowship of the JCNS. P.R. and M.M. acknowledge financial support by the Deutsche Forschungsgemeinschaft (DFG, German Research Foundation), International Collaborative Research Center No. TRR 160 (Project C9). M.M. acknowledges funding by DFG under SFB 1432 Project-ID 425217212. M.M. wishes to express her gratitude to Chuck Fadley for being a mentor on her scientific path. In 2010, a joint beamtime using the first light of the former P09 (now P22) beamline at PETRA III opened the door toward HAXPES, and this journey is ever onward.

DATA AVAILABILITY

The data that support the findings of this study are available from the corresponding author upon reasonable request.

REFERENCES

- ¹J. Mannhart and D. G. Schlom, *Science* **327**, 1607 (2010).
- ²H. Y. Hwang, Y. Iwasa, M. Kawasaki, B. Keimer, N. Nagaosa, and Y. Tokura, *Nat. Mater.* **11**, 103 (2012).
- ³M. Coll *et al.*, *Appl. Surf. Sci.* **482**, 1 (2019).
- ⁴C. Cancellieri and V. N. Strocov, *Spectroscopy of Complex Oxide Interfaces* (Springer, Berlin, 2018).
- ⁵T. S. Böschke, J. Müller, D. Bräuhäus, U. Schröder, and U. Böttger, *Appl. Phys. Lett.* **99**, 102903 (2011).
- ⁶*Ferroelectricity in Doped Hafnium Oxide: Materials, Properties and Devices*, Woodhead Publishing Series in Electronic and Optical Materials, edited by U. Schroeder, C. S. Hwang, and H. Funakubo (Woodhead, Duxford, 2019).
- ⁷G. F. Dionne, *Magnetic Oxides* (Springer US, Boston, MA, 2009).
- ⁸A. Chouprik, D. Negrov, E. Y. Tsymlal, and A. Zenkevich, *Nanoscale* **13**, 011635 (2021).
- ⁹C. S. Fadley, *Surf. Interface Anal.* **40**, 1579 (2008).
- ¹⁰C. Fadley, *J. Electron Spectrosc. Relat. Phenom.* **178–179**, 2 (2010).
- ¹¹*Hard X-ray Photoelectron Spectroscopy (HAXPES)*, 1st ed., Springer Series in Surface Sciences No. 59, edited by J. Woicik (Springer, Cham, 2016).

- ¹²M. Müller, S. Nemšák, L. Plucinski, and C. M. Schneider, *J. Electron Spectrosc. Relat. Phenom.* **208**, 24 (2016).
- ¹³E. A. Kraut, R. W. Grant, J. R. Waldrop, and S. P. Kowalczyk, *Phys. Rev. Lett.* **44**, 1620 (1980).
- ¹⁴P. G. Steeneken, L. H. Tjeng, I. Elifimov, G. A. Sawatzky, G. Ghiringhelli, N. B. Brookes, and D.-J. Huang, *Phys. Rev. Lett.* **88**, 047201 (2002).
- ¹⁵G.-X. Miao, M. Müller, and J. S. Moodera, *Phys. Rev. Lett.* **102**, 076601 (2009).
- ¹⁶M. Müller, G.-X. Miao, and J. S. Moodera, *Europhys. Lett.* **88**, 47006 (2009).
- ¹⁷P. Lömker, T. C. Rödel, T. Gerber, F. Fortuna, E. Frantzeskakis, P. Le Fèvre, F. Bertran, M. Müller, and A. F. Santander-Syro, *Phys. Rev. Mater.* **1**, 062001(R) (2017).
- ¹⁸K. J. Kormondy *et al.*, *Sci. Rep.* **8**, 7721 (2018).
- ¹⁹P. Rosenberger, M. Opel, S. Geprägs, H. Huebl, R. Gross, M. Müller, and M. Althammer, *Appl. Phys. Lett.* **118**, 192401 (2021).
- ²⁰V. Goian *et al.*, *Commun. Mater.* **1**, 74 (2020).
- ²¹R. Sutarto *et al.*, *Phys. Rev. B* **79**, 205318 (2009).
- ²²P. Lömker, "Interfacing EuO in confined oxide and metal heterostructures," Ph.D. thesis (Schriften des Forschungszentrums Jülich/Reihe Schlüsseltechnologien, Technische Universität Dortmund, 2018), p. 174.
- ²³T. Gerber, P. Lömker, B. Zijlstra, C. Besson, D. N. Mueller, W. Zander, J. Schubert, M. Gorgoi, and M. Müller, *J. Mater. Chem. C* **4**, 1813 (2016).
- ²⁴P. Rosenberger and M. Müller, "A low-dimensional model Heisenberg ferromagnet: The first monolayers of EuO/YSZ-(001)," (unpublished).
- ²⁵M. Gorgoi *et al.*, *Nucl. Instrum. Methods Phys. Res., Sect. A* **601**, 48 (2009).
- ²⁶H. Shinotsuka, S. Tanuma, C. J. Powell, and D. R. Penn, *Surf. Interface Anal.* **47**, 871 (2015).
- ²⁷J. F. Watts and J. Wolstenholme, *An Introduction to Surface Analysis by XPS and AES* (Wiley, New York, 2003).
- ²⁸P. Lömker and M. Müller, *Phys. Rev. Mater.* **3**, 061401 (2019).
- ²⁹M. H. Hamed, "Interface functionalization of magnetic oxide Fe₃O₄/SrTiO₃ heterostructures," Ph.D. thesis dissertation (Universität Duisburg, Jülich, 2021).
- ³⁰M. H. Hamed *et al.*, *ACS Appl. Mater. Interfaces* **11**, 7576 (2019).
- ³¹M. H. Hamed, D. N. Mueller, and M. Müller, *Appl. Surf. Sci. Adv.* **6**, 100132 (2021).
- ³²F. Walz, *J. Phys.: Condens. Matter* **14**, R285 (2002).
- ³³H. Elnaggar, R. Wang, M. Ghiasi, M. Yañez, M. U. Delgado-Jaime, M. H. Hamed, A. Juhin, S. S. Dhese, and F. de Groot, *Phys. Rev. Mater.* **4**, 024415 (2020).
- ³⁴H. Elnaggar, M. W. Haverkort, M. H. Hamed, S. S. Dhese, and F. M. F. de Groot, *J. Synchrotron Radiat.* **28**, 247 (2021).
- ³⁵S. Gota, E. Guiot, M. Henriot, and M. Gautier-Soyer, *Phys. Rev. B* **60**, 14387 (1999).
- ³⁶T. Fujii, F. M. F. de Groot, G. A. Sawatzky, F. C. Voogt, T. Hibma, and K. Okada, *Phys. Rev. B* **59**, 3195 (1999).
- ³⁷A. Zenkevich, Y. Matveyev, M. Minnekaev, Y. Lebedinskii, S. Thiess, and W. Drube, *J. Electron Spectrosc. Relat. Phenom.* **190**, 302 (2013).
- ³⁸C. Lenser, A. Köhl, M. Patt, C. M. Schneider, R. Waser, and R. Dittmann, *Phys. Rev. B* **90**, 115312 (2014).
- ³⁹M. Hoppe, S. Döring, M. Gorgoi, S. Cramm, and M. Müller, *Phys. Rev. B* **91**, 054418 (2015).
- ⁴⁰M. Hoppe, M. Gorgoi, C. M. Schneider, and M. Müller, *IEEE Trans. Magn.* **50**, 1 (2014).
- ⁴¹A. Gloskovskii *et al.*, *J. Electron Spectrosc. Relat. Phenom.* **185**, 47 (2012).
- ⁴²H. Lüth, *Surfaces and Interfaces of Solids*, 2nd ed., Springer Series in Surface Sciences Vol. 15 (Springer, Berlin, 1993), pp. 464–471.
- ⁴³K. van Benthem, C. Elsässer, and R. H. French, *J. Appl. Phys.* **90**, 6156 (2001).
- ⁴⁴K. Dileep, B. Loukya, N. Pachauri, A. Gupta, and R. Datta, *J. Appl. Phys.* **116**, 103505 (2014).
- ⁴⁵T. Mittmann *et al.*, *Adv. Mater. Interfaces* **6**, 1900042 (2019).
- ⁴⁶H. Kohlstedt, Y. Mustafa, A. Gerber, A. Petraru, M. Fitsilis, R. Meyer, U. Böttger, and R. Waser, *Microelectron. Eng.* **80**, 296 (2005).

- ⁴⁷F. P. G. Fengler, M. Pešić, S. Starschich, T. Schneller, U. Böttger, T. Schenk, M. H. Park, T. Mikolajick, and U. Schroeder, "Comparison of hafnia and PZT based ferroelectrics for future non-volatile FRAM applications," in *2016 46th European Solid-State Device Research Conference (ESSDERC)*, 12–15. Sept. 2016, Lausanne, Switzerland (IEEE, 2016), pp. 369–372.
- ⁴⁸M. Pešić *et al.*, *Adv. Funct. Mater.* **26**, 4601 (2016).
- ⁴⁹C. Schlueter *et al.*, *AIP Conf. Proc.* **2054**, 040010 (2019).
- ⁵⁰J. C. Hackley and T. Gougousi, *Thin Solid Films* **517**, 6576 (2009).
- ⁵¹T. Mittmann *et al.*, *Phys. Status Solidi RRL* **15**, 2100012 (2021).
- ⁵²S. Suzer, S. Sayan, M. M. Banaszak Holl, E. Garfunkel, Z. Hussain, and N. M. Hamdan, *J. Vac. Sci. Technol. A* **21**, 106 (2003).
- ⁵³T. Szyjka, L. Baumgarten, T. Mittmann, Y. Matveyev, C. Schlueter, T. Mikolajick, U. Schroeder, and M. Müller, *ACS Appl. Electron. Mater.* **2**, 3152 (2020).
- ⁵⁴M. Lee, Z.-H. Lu, W.-T. Ng, D. Landheer, X. Wu, and S. Moisa, *Appl. Phys. Lett.* **83**, 2638 (2003).
- ⁵⁵A. Glaser, S. Surnev, F. Netzer, N. Fateh, G. Fontalvo, and C. Mitterer, *Surf. Sci.* **601**, 1153 (2007).
- ⁵⁶L. Baumgarten, T. Szyjka, T. Mittmann, M. Materano, Y. Matveyev, C. Schlueter, T. Mikolajick, U. Schroeder, and M. Müller, *Appl. Phys. Lett.* **118**, 032903 (2021).
- ⁵⁷N. C. Saha and H. G. Tompkins, *J. Appl. Phys.* **72**, 3072 (1992).
- ⁵⁸C. Ernsberger, J. Nickerson, A. E. Miller, and J. Moulder, *J. Vac. Sci. Technol. A* **3**, 2415 (1985).
- ⁵⁹H. Fujisawa, S. Hyodo, K. Jitsui, M. Shimizu, H. Niu, H. Okino, and T. Shiosaki, *Integr. Ferroelectr.* **21**, 107 (1998).
- ⁶⁰T. Szyjka, L. Baumgarten, T. Mittmann, Y. Matveyev, C. Schlueter, T. Mikolajick, U. Schroeder, and M. Müller, *Phys. Status Solidi RRL* **15**, 2100027 (2021).